

# Characterising Polariton States in Non-Dispersive Regime of Circuit Quantum Electrodynamics

Arvind Mamgain, Samarth Hawaldar, Athreya Shankar, and Baladitya Suri

*Department of Instrumentation and Applied Physics, Indian Institute of Science, Bengaluru, India*

(Dated: February 10, 2023)

A superconducting qubit coupled to a read-out resonator is currently the building block of multiple quantum computing as well as quantum optics experiments. A typical qubit-resonator system is coupled in the dispersive regime, where the detuning between qubit and resonator is much greater than the coupling between them. In this work, we fabricated and measured a superconducting transmon-resonator system in the non-dispersive regime. The dressed states formed by the mixing of the bare qubit and resonator states can be further mixed by applying a drive on the qubit, leading to the formation of polariton states. We report experimental studies of transitions between polariton states at varying driving powers and frequencies and show how the non-dispersive coupling of the higher levels of the qubit-resonator system modifies the polariton eigenstates and the corresponding transition frequencies. We also report close agreement with numerical results obtained from a driven Jaynes-Cummings Model beyond the dispersive regime.

## I. INTRODUCTION

Circuit quantum electrodynamics (cQED) is an excellent testbed for the study of various light-matter, and matter-matter interaction phenomena [1–4]. A basic building block of cQED architectures consists of a microwave resonator coupled to an artificial atom, both of which are realized on a chip using superconducting microwave circuits. The atom-resonator unit forms a multi-level quantum system which can be controlled by applying microwave drives. Besides forming the basis for superconducting qubits for use in quantum computing, cQED systems are also attractive from a quantum optics perspective because they can be tuned into regimes beyond what is easily achievable, or even feasible, with natural atoms [3, 5]. Examples of such phenomena explored via cQED include the implementation of strong [1, 6], ultra-strong [7, 8], and deep strong [9] regimes of atom-cavity (resonator) coupling, probing the photon-number nonlinearity of Jaynes-Cummings (JC) systems [10–12], and single atom lasing [13]. The JC nonlinearity induced by a superconducting qubit in a resonator has also been used to implement a high-fidelity read-out [14–16].

Additional tunability of cQED systems can be introduced via the application of drive fields. By driving the  $\Xi$  (ladder) type transitions in an artificial atom, Mollow triplets [17], Autler-Townes Splitting (ATS) [17–19], and electromagnetically induced transparency (EIT) [20–22] have been probed and a single-photon router [23] has been implemented. Additionally, a  $\Lambda$ -type level structure has been realised in a qubit-resonator system using drives on both qubit-like and resonator-like transitions [24, 25]. These  $\Lambda$  systems have been used to measure the coherence of a dark state [25], coherence of high-Q resonators by probing EIT with a sideband drive on the atom [26], and to detect single microwave photons [27].

In particular, “polariton” states, which are superpositions of qubit-resonator dressed states caused by additional drive fields, have been studied in [28–32]. The tunability of frequencies and decay rates of transitions

between polariton states has been used to implement an impedance-matched  $\Lambda$ -system [30], which has been subsequently used for down-conversion and detection of microwave photons [27, 31, 32]. Polariton states have also been proposed for implementing a two-qubit gate between a superconducting and a flying qubit in a coplanar waveguide [33].

In this article, we report spectroscopic measurements of polariton states formed by driving a transmon artificial atom [34] that is in turn coupled to a lumped-element resonator. In particular, we engineer our system in a “non-dispersive” regime, where the coupling ( $g_1$ ) of the first-to-second excited state transition of the transmon to the resonator mode is comparable to the detuning ( $\Delta_1$ ) between the resonator and the transition frequencies. This is in contrast to previous works [29, 32] in which polariton states were observed in the “dispersive” regime, where the coupling between the transmon and the resonator is considerably smaller compared to the detuning for all relevant transitions of the transmon. By means of eigenmode analysis and master equation calculations, we simulate the polariton transitions and observe close agreement with experiment. We also explain the qualitative differences between polariton transitions in the dispersive and non-dispersive regimes using perturbative calculations.

The paper is organized as follows. In section II, we describe the Hamiltonian of a transmon-resonator system including a drive field on the transmon. We discuss how our device differs from typical dispersively coupled transmon-resonator systems and introduce the concept of polariton states. In section III, we describe the experimental setup used to characterise the device we fabricated. In section IV, we discuss the experimentally measured polariton spectra obtained for varying powers and frequencies of the drive tone. We demonstrate very close agreement of the measured spectra with results obtained from an eigenmode analysis as well as full master equation simulations. In section V, we qualitatively explain the behaviour of polariton transitions in

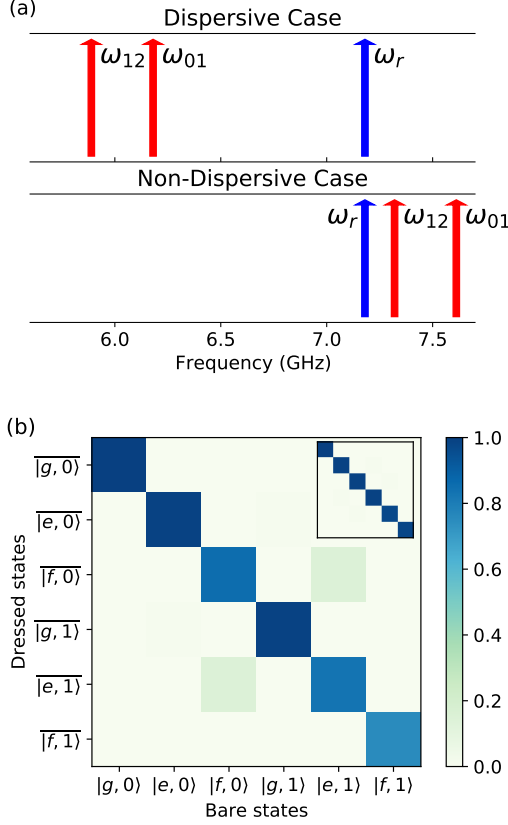


FIG. 1. (a) Frequency of bare resonator and qubit for non-dispersive and dispersive case, (b) Comparison of mixing of bare states to form dressed states in the non-dispersive limit ( $g_1/\Delta_1 = 0.47$ ) inset in the plot show the case of the dispersive limit ( $g_0/\Delta_0 = -0.108$ ,  $g_1/\Delta_1 = -0.091$ )

the non-dispersive regime using perturbation theory, and compare it to the usual dispersive case. We conclude with a summary.

## II. THEORETICAL MODEL

We consider a system consisting of a fixed-frequency transmon coupled to a lumped-element resonator, which can be described by the generalised Jaynes-Cummings Hamiltonian as [34]

$$\hat{H} = \hbar\omega_r\hat{a}^\dagger\hat{a} + \hbar\sum_j\omega_j|j\rangle\langle j| + \hbar g_0(\hat{a}^\dagger\hat{b} + \hat{a}\hat{b}^\dagger). \quad (1)$$

Here,  $\omega_r$  is the bare frequency of the resonator,  $\hbar\omega_j$  is the energy of the  $j^{\text{th}}$  excited state ( $|j\rangle$ ) of the transmon and  $g_0$  is the transmon-resonator coupling strength. The excitation (de-excitation) of the transmon and the resonator are respectively described by the creation (annihilation) operators  $\hat{b}^\dagger$  ( $\hat{b}$ ) and  $\hat{a}^\dagger$  ( $\hat{a}$ ). In writing Eq. (1), we have used the rotating-wave approximation (RWA) to neglect the rapidly oscillating terms. In our discussion, we will

use the labels  $g, e, f$  to refer to the three lowest transmon levels with  $j = 0, 1, 2$ .

Typical transmon-resonator systems operate in the so-called dispersive regime, where the coupling strength is small compared to the detuning between the transmon transition frequencies and the resonator frequency. This condition can be expressed as  $g_j/\Delta_j \ll 1$  for all energy levels  $j$ , where  $g_j \approx g_0\sqrt{j+1}$  and  $\Delta_j = \omega_{j,j+1} - \omega_r$  is the detuning of the resonator from the  $|j\rangle \rightarrow |j+1\rangle$  transition with corresponding frequency  $\omega_{j,j+1} = \omega_{j+1} - \omega_j$ . The negative anharmonicity of the transmon implies that  $\omega_{j,j+1} < \omega_{j-1,j}$ . For a transmon, the dispersive regime is usually realised by designing  $\omega_{01} < \omega_r$  (see Fig. 1).

However, in the case of our device, the transmon frequency is greater than the resonator frequency, such that the frequency for the  $|e\rangle \rightarrow |f\rangle$  transition of the transmon falls near the resonator frequency, as shown in Fig. 1. This leads to  $g_1/\Delta_1 \approx 0.47$ , for which the dispersive approximation does not hold. The strong coupling of the higher level to the resonator leads to qualitative changes in the nature of the dressed states of the system, which we discuss below.

### A. Singly dressed states

The eigenstates of the undriven transmon-resonator Hamiltonian are the “singly” dressed states formed by the mixing of the bare transmon and resonator eigenstates, see Fig. 2(a) and (b). In the dispersive regime, the transmon-resonator coupling essentially serves to modify the bare transmon and resonator frequencies, but does not cause significant mixing of the corresponding eigenstates. As a result, the dressed states are, to very good approximation, just the bare eigenstates. This is numerically demonstrated in the inset of Fig. 1, where we plot the contribution of bare states to the different dressed states in the dispersive regime.

The dressed states involving the lowest two transmon levels can be written in the dispersive regime as

$$\begin{aligned} \overline{|g, n\rangle} &= |g, n\rangle - \frac{g_0\sqrt{n}}{\Delta_0} |e, n-1\rangle \\ \overline{|e, n-1\rangle} &= |e, n-1\rangle + \frac{g_0\sqrt{n}}{\Delta_0} |g, n\rangle. \end{aligned} \quad (2)$$

Here,  $\overline{|g, n\rangle}$  and  $\overline{|e, n-1\rangle}$  are the first and second dressed states with  $n$  total excitations in the coupled transmon-resonator system. In the basis given by  $\overline{|g, n\rangle}, \overline{|e, n-1\rangle}$  with  $n = 0, 1, \dots$ , the transmon-resonator Hamiltonian in the dispersive regime can be approximated as

$$\hat{H}_{\text{disp}} = \hbar\omega'_r\hat{a}^\dagger\hat{a} + \hbar\omega'_{01}\hat{\sigma}_z + \hbar\chi\hat{\sigma}_z\hat{a}^\dagger\hat{a}. \quad (3)$$

Defining  $\chi_{j,j+1} \equiv g_j^2/\Delta_j$ , the frequencies appearing in Eq. (3) are given by  $\omega'_r = \omega_r - \chi_{12}/2$ ,  $\omega'_{01} = \omega_{01} + \chi_{01}$  and  $\chi = \chi_{01} - \chi_{12}/2$  [34].

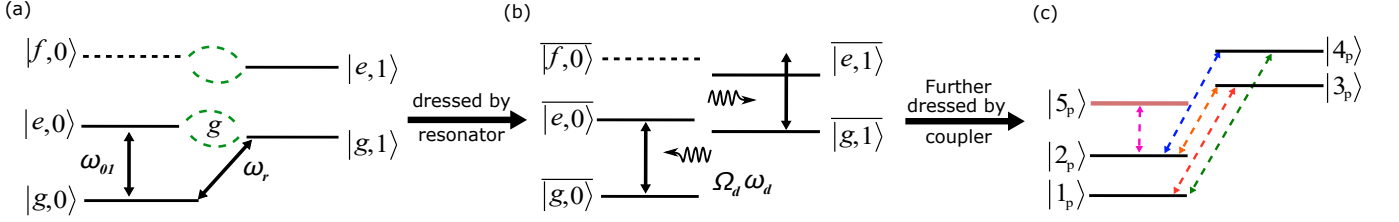


FIG. 2. Energy level diagrams showing (a) bare states of a qubit-resonator (b) dressed states of qubit-resonator showing the coupler drive (c) 5 polariton states formed for a coupler drive resonant with  $|g, 0\rangle$  to  $|e, 0\rangle$  transition with dashed arrows showing transitions between them

In the case of non-dispersive coupling, no simple closed-form expressions exist for the dressed states and hence we turn to numerical inquiries to find the eigenenergies and eigenstates of the system. In Fig. 1(b), we plot the contribution of bare (uncoupled) transmon-resonator eigenstates to the dressed states for the parameters of our device. In contrast to the dispersive case (inset), we observe a substantial contribution of the higher excited state  $|f, 0\rangle$  to the dressed state  $|\overline{e}, 1\rangle$ .

### B. Doubly dressed states: Polariton states

In order to tune the Hamiltonian and introduce further structure to the levels, we introduce a coupler drive on the transmon. This drive further dresses the states, and the resultant “doubly” dressed states are called polariton states [see Fig. 2(b) and (c)]. [28] In the presence of the coupler drive, the system Hamiltonian can be written in the rotating frame of the drive under the RWA as

$$H_{\text{rot}} = \hbar \delta_r \hat{a}^\dagger \hat{a} + \hbar \sum_n \delta_n |n\rangle \langle n| + \hbar g_0 (\hat{a}^\dagger \hat{b} + \hat{a} \hat{b}^\dagger) + \hbar \Omega_d (\hat{b} + \hat{b}^\dagger). \quad (4)$$

Here, the drive has frequency  $\omega_d$  and Rabi frequency  $\Omega_d$ , and we have introduced  $\delta_n = \omega_n - n\omega_d$ ,  $\delta_r = \omega_r - \omega_d$ .

In the dispersive regime, for weak to moderate drive powers (i.e.  $\Omega_d$ ), four polariton states are formed by mixing the four lowest energy singly dressed states as [28]

$$\begin{pmatrix} |1_p\rangle \\ |2_p\rangle \\ |3_p\rangle \\ |4_p\rangle \end{pmatrix} = \begin{pmatrix} R_{\frac{\theta_0}{2}} & 0 \\ 0 & R_{\frac{\theta_1}{2}} \end{pmatrix} \begin{pmatrix} |\overline{g}, 0\rangle \\ |\overline{e}, 0\rangle \\ |\overline{e}, 1\rangle \\ |\overline{g}, 1\rangle \end{pmatrix}, \quad (5)$$

where

$$R_\theta = \begin{pmatrix} \cos \theta & -\sin \theta \\ \sin \theta & \cos \theta \end{pmatrix}$$

and  $\tan \theta_{0(1)} = 2\Omega_d / (\omega'_{ge,0(1)} - \omega_d)$  where  $\omega'_{ge,n}$  is the frequency of the  $|\overline{g}, n\rangle \rightarrow |\overline{e}, n\rangle$  transition. In the case of our non-dispersively coupled device, we rely on numerical calculations to relate the polariton states to the singly dressed states.

### C. Probing polariton transitions

In our experiment, we probe the transition frequencies between various polariton states by introducing a weak probe that induces resonator-like transitions, i.e.  $|1_p\rangle \rightarrow |3_p\rangle$ ,  $|1_p\rangle \rightarrow |4_p\rangle$ ,  $|2_p\rangle \rightarrow |3_p\rangle$  and  $|2_p\rangle \rightarrow |4_p\rangle$ . The corresponding Hamiltonian is given by  $H_{\text{probe}} = \Omega_p (ae^{i\omega_p t} + a^\dagger e^{-i\omega_p t})$ .

In the dispersive regime, these transition frequencies are given by

$$\begin{aligned} \omega_{13,p} &= \omega'_r - \chi - (\sqrt{\chi^2 + \Omega_d^2} - \Omega_d), \\ \omega_{14,p} &= \omega'_r - \chi + (\sqrt{\chi^2 + \Omega_d^2} + \Omega_d), \\ \omega_{23,p} &= \omega'_r - \chi - (\sqrt{\chi^2 + \Omega_d^2} + \Omega_d), \\ \omega_{24,p} &= \omega'_r - \chi + (\sqrt{\chi^2 + \Omega_d^2} - \Omega_d). \end{aligned} \quad (6)$$

For the case of non-dispersive coupling or strong coupler drive, higher levels of the transmon start to contribute significantly to the polariton states. Experimentally observed transitions between these polariton states and comparisons with theoretically predicted transition frequencies and intensities will be discussed in detail in Section IV. For the latter, we note that the intensity of an observed transition between states  $|\alpha\rangle$ ,  $|\beta\rangle$  is proportional to

$$I_{|\alpha\rangle \leftrightarrow |\beta\rangle} \propto (P_\alpha + P_\beta) |\langle \alpha | a | \beta \rangle|^2, \quad (7)$$

where  $P_\alpha, P_\beta$  are the steady-state occupations of the states  $|\alpha\rangle$  and  $|\beta\rangle$  and  $|\langle \alpha | a | \beta \rangle|$  is the probe-induced transition matrix element.

## III. EXPERIMENTAL SETUP

A schematic of the measurement setup is shown in Fig. 3. A fixed-frequency transmon capacitively coupled to a lumped-element resonator is mounted at the 15mK stage of a dilution refrigerator. The resonator, in turn, is coupled to a coplanar waveguide transmission line (CPW) to control and probe the device. The initial characterization of the device is performed using Jaynes-Cummings readout [14] in order to obtain the transition

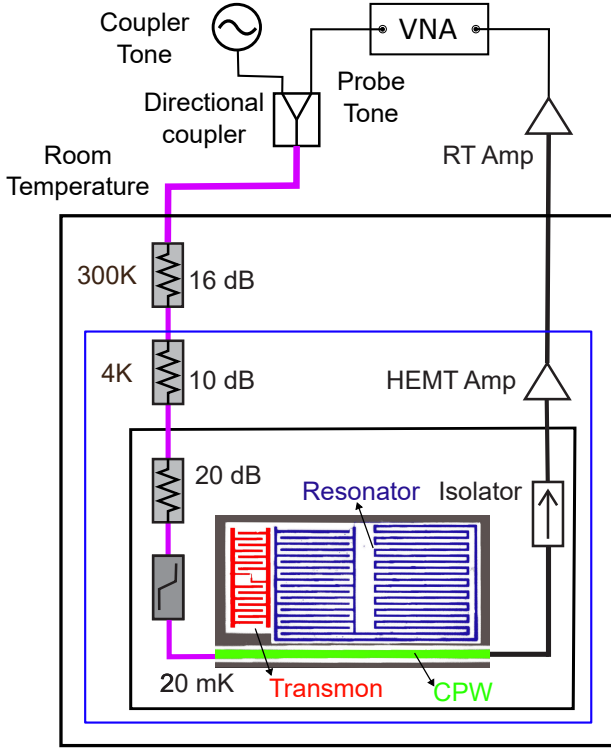


FIG. 3. Schematic diagram of the measurement setup. Inset shows an SEM image of the measured device (with false color) including a quasi-lumped-element resonator and a transmon with an interdigitated capacitor.

frequencies and the coherence times ( $T_1$  and  $T_2^*$ ) of the qubit. All the experimentally measured parameters of the device are given in Table I. The probe and coupler tones used in the spectroscopic measurements of polariton transitions are combined using a directional coupler and input to the CPW of the device as shown in Fig. 3. The transmitted signal coming out of the output port is then measured with the VNA after amplifying it using a high electron-mobility transistor (HEMT) amplifier at the 4K stage followed by room temperature (RT) amplifiers.

In this work, we study the polariton transitions as a function of varying coupler drive-strength. For each coupler power, we fix the frequency of the coupler tone at  $\omega_{\text{coup}} = \omega'_{ge,0}$ , the dressed frequency of the qubit with zero photons in the resonator, and sweep the frequency of a weak probe tone to measure the transmission coefficient  $|S_{21}|$ . The probe frequency is swept across the “mean frequency”  $\omega'_{r,\text{mid}} = (\omega'_{r,e} + \omega'_{r,g})/2$ , where  $\omega_{r,e(g)}$  is the singly dressed frequency of the resonator when the transmon is in the first-excited (ground) state. We vary the coupler powers from  $-80$  dBm to  $0$  dBm at the source ( $\approx -126$  dBm to  $-56$  dBm at the device) (see Fig. 4). We also perform polariton spectroscopy as we vary the coupler frequency while keeping the coupler power fixed (see Fig. 6).

Bare resonator frequency	$\omega_r/2\pi$	7.180 GHz
Dressed resonator frequency	$\omega'_{r,0}/2\pi$	7.175 GHz
Coupling	$g/2\pi$	46.57 MHz
Anharmonicity	$\alpha/2\pi$	-291.8 MHz
Dressed qubit frequency with 0 photons in resonator	$\omega'_{ge,0}/2\pi$	7.616 GHz
Dressed qubit frequency with 1 photon in resonator	$\omega'_{ge,1}/2\pi$	7.599 GHz
Dressed resonator frequency with qubit in ground state	$\omega'_{r,g}/2\pi$	7.175 GHz
Dressed resonator frequency with qubit in excited state	$\omega'_{r,e}/2\pi$	7.158 GHz
Qubit decay rate	$1/T_1 = \Gamma_1$	$1.11 \mu\text{s}^{-1}$
Qubit dephasing rate	$1/T_\varphi = \Gamma_\varphi$	$1.32 \mu\text{s}^{-1}$
Resonator decay rate	$\kappa$	$3.09 \mu\text{s}^{-1}$

TABLE I. Device parameters

#### IV. OBSERVATIONS AND DISCUSSION

Figure 4(a) shows the spectroscopy of polariton transitions for a fixed coupler frequency of  $\omega_{\text{coup}} = \omega'_{ge,0}$ , as the coupler power is varied. The observed data can be classified into four regimes of coupler power, *viz.*, very low power ( $< -70$  dBm), low power ( $-70$  dBm -  $-45$  dBm), moderate power ( $-45$  dBm -  $-15$  dBm) and high power ( $> -15$  dBm) regimes.

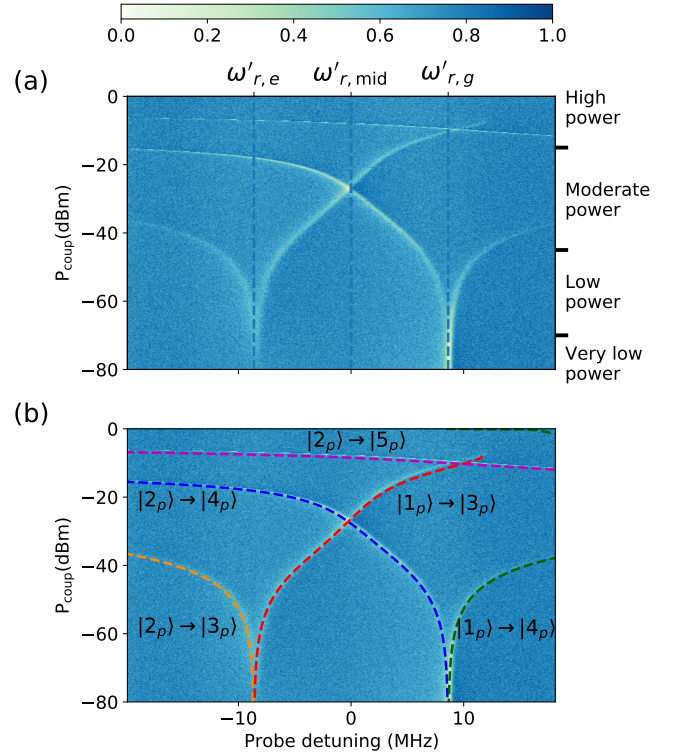


FIG. 4. Polariton state spectroscopy with coupler drive power varied at  $\omega_{\text{coup}} = \omega'_{ge,0}$ , dashed lines in bottom plot show the simulated transition frequencies.

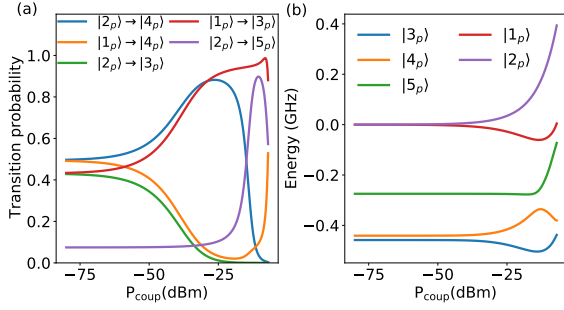


FIG. 5. (a) Shows transition probability all five visible transitions due to probe drive (b) energy of polariton states varying with the power of coupler drive in dressed frame.

In Fig. 4(b), we overlay the measured data with results from an eigenmode calculation, which enables us to identify the various polaritonic transitions. Furthermore, we are able to qualitatively predict the intensity and linewidths of the observed lines using a full master equation simulation. The details of the eigenmode calculation and the master equation simulations are presented in Appendix B. In the following, we qualitatively explain the features observed in the experiment using the energies of the polariton states and the transition probabilities between these states, which are plotted as a function of coupled power in Fig. 5.

### A. Very low power regime

In the very low power regime, one observes only one line, which occurs at  $\omega'_{r,g}$ , i.e. the dressed resonator frequency with transmon in the ground state. Here, only the state  $|g,0\rangle$  has a significant steady-state occupation, and the observed line corresponds to the  $|g,0\rangle \rightarrow |g,1\rangle$  transition induced by the probe. In terms of polariton states, this corresponds to  $|1_p\rangle \rightarrow |4_p\rangle$  and  $|2_p\rangle \rightarrow |4_p\rangle$  transitions which are almost degenerate in this regime.

### B. Low power regime

As the coupler power is increased, we move into the low power regime, where a second line appears. This line occurs at  $\omega'_{r,e}$ , i.e. the dressed resonator frequency with transmon in the first-excited state, indicating that as the drive power increases, the state  $|e,0\rangle$  begins to get populated. To explain the two lines in terms of polariton states, we note that the non-dispersive nature of the higher transmon levels enhances the dispersive shift  $\chi \approx (\omega'_{ge,0} - \omega'_{ge,1})/2 \approx 2\pi \times 8.5$  MHz. The system in this regime can be analyzed within the two-level dispersive approximation, but using the measured value of  $\chi$  in Eq. (6). For low drive powers such that  $\Omega_d^2/\chi^2 \ll 1$ , the

transition frequencies are approximately given by

$$\begin{aligned}\omega_{13,p} &= \tilde{\omega}_r - 2\chi + \Omega_d, \\ \omega_{14,p} &= \tilde{\omega}_r + \Omega_d, \\ \omega_{23,p} &= \tilde{\omega}_r - 2\chi - \Omega_d, \\ \omega_{24,p} &= \tilde{\omega}_r - \Omega_d.\end{aligned}\quad (8)$$

Eq. (8) explains why only two lines are initially visible in the low power regime. To resolve any two transitions, the frequency difference between them should be greater than the resonator linewidth  $\kappa/2\pi \approx 491$  kHz. The two spectral lines observed correspond to the nearly degenerate, and hence unresolved pairs of transitions  $|1_p\rangle \rightarrow |3_p\rangle, |2_p\rangle \rightarrow |3_p\rangle$  and  $|1_p\rangle \rightarrow |4_p\rangle, |2_p\rangle \rightarrow |4_p\rangle$ , which only differ by  $\sim \Omega_d \lesssim \kappa$ . This can also be seen in Fig 5(b) where the states  $|1_p\rangle$  and  $|2_p\rangle$ , and hence the above mentioned transitions, are nearly degenerate.

We also observe that the line around  $\omega'_{r,g}$  is brighter than the one around  $\omega'_{r,e}$ . This can be explained by noting that, at low drive power and in the presence of transmon and resonator dissipation, the steady state population is predominantly in the ground state  $|g,0\rangle$ .

With a further increase in power, the degeneracy of the  $|1_p\rangle$  and  $|2_p\rangle$  states, and hence of the two pairs of transitions, is lifted (see Fig. 5), and we observe four distinct lines.

### C. Moderate power regime

As one starts to move into the moderate power regime, we observe that the intensities of the  $|1_p\rangle \rightarrow |4_p\rangle$  and  $|2_p\rangle \rightarrow |3_p\rangle$  lines start to diminish. This agrees with the behavior of the corresponding transition probabilities,  $|\langle \alpha | a | \beta \rangle|^2$ , which decrease with an increase in the coupler power, as seen in Fig. 5(b). Therefore only the  $|1_p\rangle \rightarrow |3_p\rangle$  and  $|2_p\rangle \rightarrow |4_p\rangle$  transitions are visible as the drive power increases.

In this regime, the dispersive two-level approximation breaks down for our system. Equations (6) predict that the  $|1_p\rangle \rightarrow |3_p\rangle$  and  $|2_p\rangle \rightarrow |4_p\rangle$  transition frequencies only asymptotically converge as the drive power is increased. Contrary to this prediction, we observe a distinct crossing of the two lines around a drive power of  $-26$  dBm. The presence of a distinct crossing can be qualitatively explained by the unusually large value of  $\chi$  in our device, which is made possible by the non-dispersive coupling of the higher transmon levels to the resonator. We discuss this in greater detail in Sec. V.

### D. High power regime

As one increases the power of the coupler drive even further, going into the high-power regime, a fifth line is observed (see Fig. 4). This fifth line can be explained using Fig. 5(b), where the transition probability between  $|2_p\rangle$  and a fifth polariton state  $|5_p\rangle$  becomes appreciable



at high drive powers. Furthermore, the frequency of this transition falls within the probed range of frequencies only at high powers. The crossing between  $|2_p\rangle \rightarrow |5_p\rangle$  and  $|1_p\rangle \rightarrow |3_p\rangle$  transitions around  $-10$  dBm is also predicted by numerical calculations of the polariton state energies as seen in Fig. 4(b).

### E. Spectroscopy at different coupler frequencies

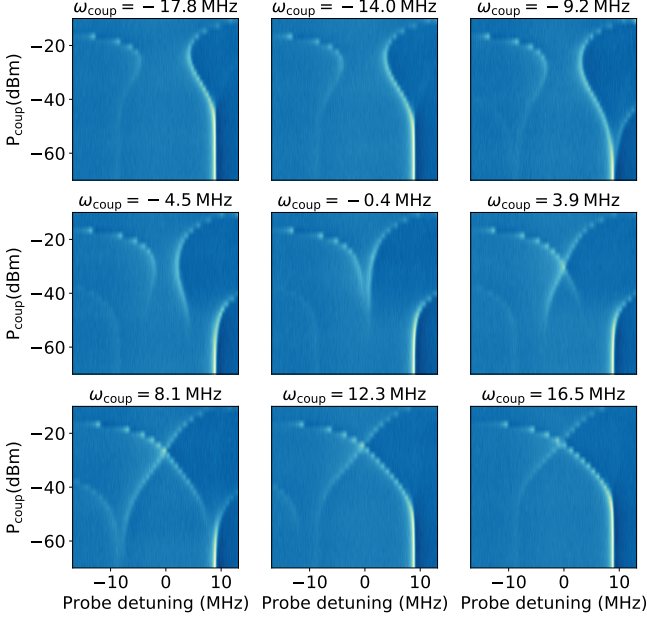


FIG. 6. Spectroscopy plot at different frequencies of coupler drive detunings

Previously, we discussed spectroscopic measurements when the coupler drive frequency  $\omega_{\text{coup}}$  was resonant with the  $|g, 0\rangle \rightarrow |e, 0\rangle$  transition. Here we consider polariton spectra measured with different values of  $\omega_{\text{coup}}$ , as shown in Fig. 6. From these plots, we observe that the crossing between the  $|1\rangle \rightarrow |3\rangle$  and  $|2\rangle \rightarrow |4\rangle$  lines can be observed only for  $\omega_{\text{coup}} \gtrsim (\omega'_{ge,0} + \omega'_{ge,1})/2$ . This observation is consistent with our numerical simulations (see Appendix C).

In order to gain further insight into the effect of coupler tone frequency, we performed spectroscopy of the polariton states by sweeping the coupler frequency while keeping the coupler power fixed. The measured data for a coupler power of  $-40$  dBm is shown in Fig. 7(a) and a comparison with the eigenmode calculation is shown in Fig. 7(b). We observe that the spectrum at a coupler tone frequency  $\omega_{\text{coup}} = (\omega'_{ge,0} + \omega'_{ge,1})/2$  resembles a Mollow triplet. This value of  $\omega_{\text{coup}}$  corresponds to the point where  $|1_p\rangle \rightarrow |3_p\rangle$  and  $|2_p\rangle \rightarrow |4_p\rangle$  transitions become degenerate. Moreover, the triplet is observed at this specific value of  $\omega_{\text{coup}}$  for a broad range of drive powers. At coupler frequencies away from this point, we

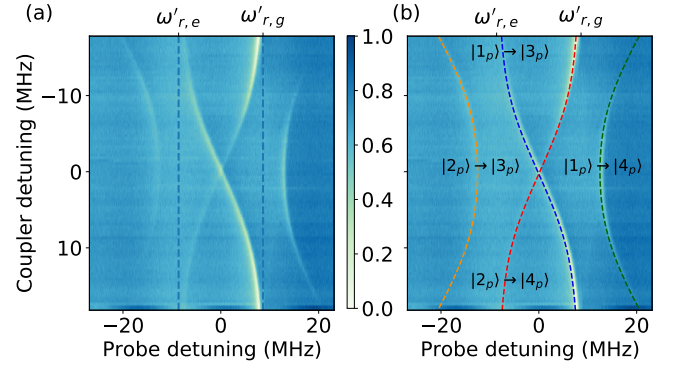


FIG. 7. Polariton state spectroscopy with  $\omega_{\text{coup}}$  varied at coupler drive power of  $-40$  dBm

observe four lines in the spectrum corresponding to the four polaritonic transitions.

## V. COMPARISON WITH DISPERSIVE CASE

In this section, we discuss the role of the non-dispersive coupling of the higher transmon levels in the observed spectroscopic data.

### A. Master equation simulations

First, we qualitatively compare master equation simulations of our device in the non-dispersive regime, with a typical transmon-resonator system in the dispersive regime, where the bare transmon frequency is 1 GHz below the resonator, as shown in Fig. 1. All other parameters are the same for both systems and are listed in Table I.

The simulated spectra for the two systems are shown in Fig. 8. The location of the lines, their intensities, and linewidths in Fig. 8(a) are consistent with the measured data shown in Fig. 4. A noticeable difference between the spectra in Fig. 8(a) and (b) is the absence of a distinct crossing of the lines in the latter case. Instead, we observe the two lines approaching each other in frequency, becoming indistinguishable beyond  $-55$  dBm of coupler power.

### B. Qualitative explanation for distinct crossing

The observation of a distinct crossing in the experiment is the result of a large value of  $\chi$  which, in our device, originates from the non-dispersive coupling of the  $|e\rangle \rightarrow |f\rangle$  transition to the resonator. Despite the non-dispersive origin of this large  $\chi$ , we can qualitatively predict a crossing through analytical calculations in a multi-level dispersive approximation, while using a large value of  $\chi$ . To do so, we extend the work of Ref. [28] to include

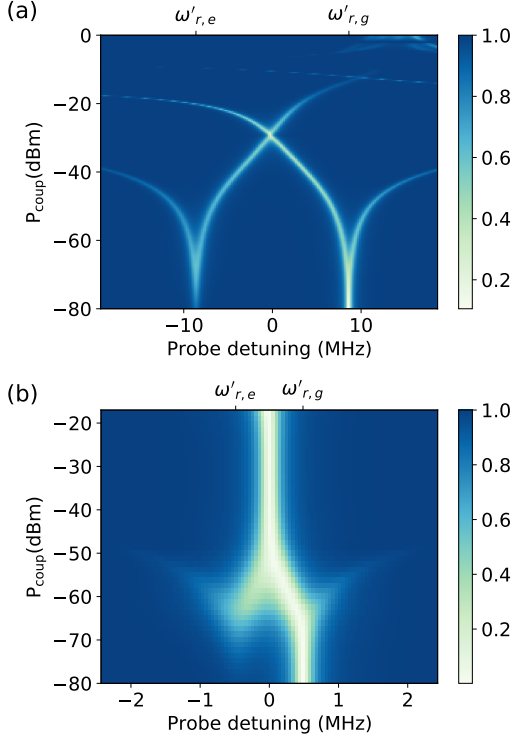


FIG. 8. Master Equation simulation of spectroscopy of the system with (a) Non-Dispersive Coupling, (b) Dispersive Coupling

the effect of higher levels along the lines of Ref. [34]. The central idea is that, for the data shown in Fig. 4, the coupler drive frequency is near-resonant with  $|g, n\rangle \rightarrow |e, n\rangle$  transitions but off-resonant from  $|e, n\rangle \rightarrow |f, n\rangle$  transitions. This is because of the fact that, for moderate drive powers, we have  $\Omega_d \ll \alpha$  where  $\alpha = \omega_{e,f} - \omega_{g,e}$  is the anharmonicity of the transmon. As a result, the off-resonant driving of higher transmon transitions by the coupler can be treated using perturbation theory. The details of this calculation are presented in Appendix D. Using this approach, we find that the frequencies of the  $|1_p\rangle \rightarrow |3_p\rangle$  and  $|2_p\rangle \rightarrow |4_p\rangle$  polaritonic transitions are given by

$$\begin{aligned} \omega_{13,p} &= \tilde{\omega}_r - \chi - (\sqrt{\chi^2 + \Omega_d^2} - \Omega_d) + \frac{\Omega_d^2 \cos \theta_1}{\alpha}, \\ \omega_{24,p} &= \tilde{\omega}_r - \chi + (\sqrt{\chi^2 + \Omega_d^2} - \Omega_d) - \frac{\Omega_d^2 \cos \theta_1}{\alpha}, \end{aligned} \quad (9)$$

where  $\tan \theta_1 = -\Omega_d/\chi$ . The two frequencies become degenerate ( $\omega_{13,p} = \omega_{24,p}$ ) when

$$\sin \theta_1 + \frac{\Omega_d \sin(2\theta_1)}{2\alpha} = 1. \quad (10)$$

The two-level case can be obtained as the limit when  $\alpha \rightarrow \infty$ . In this case, the crossing condition becomes  $\theta_1 = \pi/2$ , which is only satisfied as  $\Omega_d \rightarrow \infty$  and hence the crossing is not observed.

For a multi-level system like a transmon, where  $\alpha$  is finite, we can obtain an approximate crossing condition from Eq. (10). For  $\Omega_d^2 \gg \chi^2$ , we can substitute  $\sin \theta_1 \approx 1 - \chi^2/(2\Omega_d^2)$ ,  $\cos \theta_1 \approx -\chi/\Omega_d$  in Eq. (10) and obtain the crossing condition  $\Omega_d^2 \approx -\chi\alpha/2$ . In addition, in order to observe a distinct crossing, we require that the crossing condition must be satisfied for drive powers such that the two transitions are well resolved. Since the resolution of the observed transitions is limited by the resonator linewidth  $\kappa$ , the two transitions are resolvable when their frequency difference close to the crossing is greater than  $\kappa$ , i.e.  $\sqrt{\chi^2 + \Omega_d^2} - \Omega_d > \kappa$ . By substituting the crossing condition  $\Omega_d^2 \approx -\chi\alpha/2$  into this inequality, we arrive at the condition  $|\chi| \gtrsim (\kappa\sqrt{2|\alpha|})^{2/3}$  that satisfies both the above requirements.

For a transmon-resonator system with typical values of  $\alpha/2\pi \sim -300$  MHz and  $\kappa/2\pi \sim 0.5 - 10$  MHz, this leads to a required value of  $\chi/2\pi \gtrsim 5.3 - 39$  MHz. In our device, the non-dispersive coupling of the upper transmon levels to the resonator leads to  $\chi/2\pi \approx 8.5$  MHz, which for a  $\kappa/2\pi \approx 0.5$  MHz, enables us to observe a distinct crossing. On the other hand, for a transmon system coupled in the dispersive regime, usually  $\chi/2\pi \lesssim 2$  MHz, making the observation of a distinct crossing difficult.

## VI. CONCLUSION

We theoretically and experimentally studied the properties of polariton states in a transmon-resonator system operating in a non-dispersive regime. The non-dispersive coupling arises from the fact that the frequency of  $|e\rangle \rightarrow |f\rangle$  transition of the transmon lies close to the resonator frequency, resulting in a value of  $g_1/\Delta_1 \approx 0.47$ . By introducing a coupler drive on the transmon, we generated polariton states. We spectroscopically studied the polariton transitions using a weak probe field on the resonator. By using eigenmode analysis, and master equation simulations, we were able to explain the origin of the observed spectral lines and their intensities. We found that the observed lines differed significantly from those expected in the dispersive regime. In particular, at moderate coupler drive powers, we observed a distinct crossing between two lines. Using perturbation theory, we derived a condition on  $\chi$  required to observe a crossing, and showed that the large value of  $\chi/2\pi \approx 8.5$  MHz in our device satisfied this condition. We also showed that this condition was difficult to be satisfied in the usual dispersive regime.

## ACKNOWLEDGMENTS

The authors acknowledge the support of Ministry of Electronics and Information Technology, Government of India, under the Centre for Excellence in Quantum Technology grant to Indian Institute of Science. The authors

also acknowledge support from the Department of Science and Technology, India, via the QuEST program. The authors acknowledge the fabrication and characterisation facilities NNFC and MNCF at CeNSE, IISc, as well as fabrication facilities supported by the Institute of Eminence grant to IISc by Ministry of Education, Govt. of India. AM acknowledges the support of Ministry of Education, Government of India. SH acknowledges the support of Kishore Vaigyanik Protsahan Yojana, Department of Science and Technology, Government of India. AS acknowledges the support of a CV Raman Post-Doctoral Fellowship, IISc.

### Appendix A: Device Fabrication

The device was fabricated in three steps of lithography. The first step involved patterning of the gold alignment markers. A fresh 2-inch Si wafer was coated with an optical resist S1805, spun at 4000 rpm for 45 sec and 1 minute of baking at 110°C. Then the alignment marks were written using Heidelberg direct-write laser writer followed by development using AZ786 developer. Post development, the wafer went through the process of O<sub>2</sub> plasma ashing to remove the extra photoresist. A thin film of gold was deposited using an e-beam evaporator (Leybold) followed by a liftoff process using acetone. A second step of photolithography was used to pattern the CPW transmission line, resonator and ground plane in Aluminum. The deposition of Al was done in an e-beam evaporator followed by a liftoff process using acetone. The final step of patterning the Josephson junctions involved electron beam lithography in a 30kV Raith eLINE tool. The samples were first coated with PMMA 950 C6 resist and baked for 15 minutes at 180°C. Following e-beam lithography, and development using MIBK: IPA(1:3) for 40 sec and IPA for 1 min, the Josephson junctions were formed using a bridgeless junction technique [35]. The intermediate oxidation step between the two Al depositions was done at 700 mTorr pressure for 20 min.

### Appendix B: Eigenmode analysis

We recall that the Hamiltonian in the frame of the coupler drive is given by

$$\frac{H_{\text{rot}}}{\hbar} = \delta_r \hat{a}^\dagger \hat{a} + \sum_n \delta_n |n\rangle \langle n| + g_0 (\hat{a}^\dagger \hat{b} + \hat{a} \hat{b}^\dagger) + \Omega_d (\hat{b} + \hat{b}^\dagger), \quad (\text{B1})$$

where the symbols are defined in Section II. To find the energy of polariton states, we diagonalise Hamiltonian B1. We note that the transition frequencies in the lab frame can be obtained from the eigenfrequencies of this Hamiltonian upon shifting them by the coupler frequency. This point becomes clear when computing the transition matrix elements in the presence of a probe, which is discussed below.

In the additional presence of a probe, the full Hamiltonian  $H$  of the system can be written in the frame of the coupler drive as

$$H = H_{\text{rot}} + \hbar \Omega_p (a e^{i\delta_p t} + a^\dagger e^{-i\delta_p t}), \quad (\text{B2})$$

where  $\Omega_p$  is the probe strength,  $\omega_p$  is the probe frequency, and  $\delta_p = \omega_p - \omega_d$ .

As this probe is considered to be weak, we can neglect its effect on the eigenspectrum of the Hamiltonian. However, we do not neglect in the context of transitions between eigenstates of  $H_{\text{rot}}$ , for example  $|\alpha\rangle, |\beta\rangle$  with respective energies  $\hbar\omega_\alpha, \hbar\omega_\beta$ . The corresponding transition matrix element is given by

$$\begin{aligned} \tau &= \langle \alpha(t) | (H_p/\hbar) | \beta(t) \rangle \\ &= \Omega_p (\langle \alpha | e^{i\omega_\alpha t} (a e^{i\delta_p t} + a^\dagger e^{-i\delta_p t}) (e^{-i\omega_\beta t} |\beta\rangle) \\ &= \Omega_p (e^{-i(\omega_\tau - \delta_p)t} \langle \alpha | a | \beta \rangle + e^{i(\omega_\tau - \delta_p)t} \langle \alpha | a^\dagger | \beta \rangle), \quad (\text{B3}) \end{aligned}$$

where  $\hbar\omega_\tau = \hbar(\omega_\beta - \omega_\alpha)$  is the difference between the energies of the states in the coupler drive frame. From this, we see that to obtain a non-zero time-averaged value of  $\tau$ , the probe frequency must equal the transition frequency in the lab frame, which is given by  $\omega_d + \omega_\tau$ , which is the condition for energy conservation.

### Appendix C: Details of master equation simulations

While eigenmode analysis enables us to identify the observed transitions and qualitatively predict their intensities and linewidths, in order to get a quantitative prediction, we use master equation simulations. Starting from the lab-frame Hamiltonian including both the coupler and the probe fields, we transform to an interaction picture through the unitary operator

$$U'_{\text{rot}} = e^{i\omega_p t (\hat{a}^\dagger \hat{a}) + i\omega_d t (\hat{b}^\dagger \hat{b})}, \quad (\text{C1})$$

resulting in an interaction Hamiltonian

$$\begin{aligned} \frac{H_{\text{rot}}}{\hbar} &= \delta_r \hat{a}^\dagger \hat{a} + \sum_n \delta_n |n\rangle \langle n| + \Omega_d (\hat{b} + \hat{b}^\dagger) + \Omega_p (\hat{a} + \hat{a}^\dagger) \\ &\quad + g_0 (e^{i\Delta t} \hat{a}^\dagger \hat{b} + e^{-i\Delta t} \hat{b}^\dagger \hat{a}), \quad (\text{C2}) \end{aligned}$$

where  $\Delta = \omega_p - \omega_d$ .

To include the environmental effects like the decay of transmon and resonator, the master equation simulations were performed including Lindblad terms describing the decay (rate  $\Gamma_1$ ) and dephasing ( $\Gamma_\phi$ ) of the transmon, and the decay of the resonator ( $\kappa$ ). The complete master equation is

$$\dot{\rho} = -\frac{i}{\hbar} [H_{\text{rot}}, \rho] + \kappa \mathcal{D}[a] \rho + \Gamma_1 \mathcal{D}[b] \rho + \Gamma_\phi \mathcal{D}[b^\dagger b] \rho, \quad (\text{C3})$$

where  $\mathcal{D}[A] \rho = A \rho A^\dagger - \frac{1}{2} (A^\dagger A \rho + \rho A^\dagger A)$ .



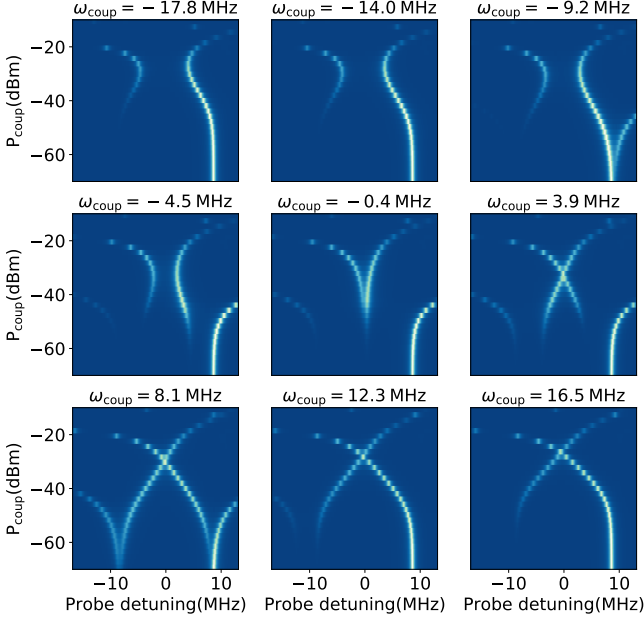


FIG. 9. Master Equation simulations corresponding to spectroscopy plot Fig. 6 at different coupler drive detunings, as described in Appendix. C

The simultaneous presence of both coupler and probe means that there is no rotating frame in which the Hamiltonian can be made time-independent. Since this equation is time-dependent, finding steady-state solutions to it can be computationally expensive. To decrease the computational resources required, we make use of the method of Matrix Continued Fractions [36, 37] as our time-dependent terms are sinusoidal with a single frequency. In this method, one rewrites the time evolution as

$$\dot{\rho} = (\mathcal{L}_0 + \mathcal{L}_1 e^{i\Delta t} + \mathcal{L}_{-1} e^{-i\Delta t})\rho, \quad (\text{C4})$$

where  $\mathcal{L}_{(-1,0,1)}$  are Liouvillians. This equation can be solved iteratively by expanding  $\rho$  into its frequency components. A recursion relation between different frequency components of  $\rho$  is obtained and after solving these equations to the desired level of accuracy, the time-independent component of the solution is considered as the steady state, since the oscillating components average to zero over time. More details on the solution can be found in [37]. A partial implementation of this method can be found in QuTiP [38] for  $\mathcal{L}_1 = \mathcal{L}_{-1}$ . For our simulations, we have extended the method to treat the case when  $\mathcal{L}_1 \neq \mathcal{L}_{-1}$ .

For our system, we write the terms in the master equation as

$$\begin{aligned} \mathcal{L}_0 &= -\frac{i}{\hbar}[H_{\text{rot},0}, \rho] + \kappa \mathcal{D}[a] + \Gamma_1 \mathcal{D}[b] + \Gamma_\phi \mathcal{D}[b^\dagger b], \\ \mathcal{L}_1 &= -\frac{i}{\hbar}[g_0 a^\dagger b, \rho], \quad \mathcal{L}_{-1} = -\frac{i}{\hbar}[g_0 a b^\dagger, \rho], \end{aligned} \quad (\text{C5})$$

where  $H_{\text{rot},0}$  is the time-independent part of the Hamiltonian  $H_{\text{rot}}$  in Eq. (C2). Solving these equations as described above, we find the time-independent steady-state component  $\rho_{\text{ss}}$  and the associated mean number of photons in the resonator mode  $\langle a^\dagger a \rangle = \text{Tr}[a^\dagger a \rho_{\text{ss}}]$ . In the experiment, we can measure the coefficient of power transmission, which is proportional to the steady state resonator occupation. Hence, we plot the latter observable as a proxy for the spectrum in our numerical simulations.

In Fig. 9, we show simulated spectra for the parameters of the experimental data presented in Fig. 6. The simulations reproduce the observed spectra very well and provide further confirmation of the accuracy of our modeling.

#### Appendix D: Perturbation theory calculations to account for higher levels in the transmon

In this appendix, we show the detailed calculations that help us explain the existence of a crossing in a multilevel non-dispersive system. To do this, we extend the work of Ref. [28] to consider the effect of higher levels in the transmon. Applying a multilevel dispersive rotation to the Hamiltonian (Eq. 4), we obtain the Hamiltonian written in the singly dressed basis as [34]

$$\begin{aligned} \frac{H_{\text{disp,rot}}}{\hbar} &\approx \sum_n \delta'_n \overline{|n\rangle\langle n|} + \delta'_r a^\dagger a - \chi_{01} a^\dagger a \overline{|0\rangle\langle 0|} \\ &+ \sum_{n>0} (\chi_{n-1,n} - \chi_{n,n+1}) a^\dagger a \overline{|n\rangle\langle n|} + \Omega_d (b + b^\dagger), \end{aligned} \quad (\text{D1})$$

where  $\delta'_n$  is the dispersively shifted energy levels of the transmon in the drive frame,  $\delta'_r$  is the dispersively shifted frequency of the resonator, and  $\chi_{i,i+1}$  are the dispersive frequency shifts between neighbouring transmon states. Here we assume that the residual drive on the dressed resonator arising from the dispersive rotation can be neglected.

For the subspace with  $r$  excitations in the resonator, we can replace  $a^\dagger a \rightarrow r$  and write the transmon part of the Hamiltonian as

$$\frac{H_{q,r}}{\hbar} = \sum_n \delta_{n,r} \overline{|n_r\rangle\langle n_r|} + \Omega_d (b + b^\dagger), \quad (\text{D2})$$

where  $\overline{|n_r\rangle} = \overline{|n, r\rangle}$  and the resonator-induced shifts have been absorbed into an effective energy  $\delta_{n,r}$  for the level  $\overline{|n_r\rangle}$ .

To simulate the experimental results presented here, we consider the case of  $\omega_{\text{coup}}$  near-resonant to  $\omega'_{ge,r} = \omega'_{01,r}$  while being far-detuned from  $\omega'_{ef,r} = \omega'_{12,r}$ . Also, for the sake of this calculation, we assume  $\Omega_d \ll \alpha$ , the anharmonicity. Hence, the effective contribution of off-resonant driving can be studied perturbatively by writing  $H_{q,r}$  as

$$H_{q,r} = H_{q,r}^0 + H_{q,r}^1, \quad (\text{D3})$$

where

$$H_{q,r}^0 = \sum_n \delta_{n,r} \overline{|n_r\rangle\langle n_r|} + \Omega_d (\overline{|0_r\rangle\langle 1_r|} + \overline{|1_r\rangle\langle 0_r|}) \quad (\text{D4})$$

is the unperturbed Hamiltonian and

$$H_{q,r}^1 = \Omega_d \sum_{n>1} \sqrt{n} (\overline{|n_r\rangle\langle (n-1)_r|} + \overline{|(n-1)_r\rangle\langle n_r|}) \quad (\text{D5})$$

is the perturbation. As a result of the coupler drive, the first two eigenstates of the unperturbed Hamiltonian are given by

$$\begin{pmatrix} \overline{|+_r\rangle} \\ \overline{|-_r\rangle} \end{pmatrix} = R_{\frac{\theta_r}{2}} \begin{pmatrix} \overline{|0_r\rangle} \\ \overline{|1_r\rangle} \end{pmatrix} \quad (\text{D6})$$

where  $\tan \theta_r = 2\Omega_d/\delta_{1,r}$ , while the other eigenstates are  $\overline{|n_r\rangle}$  for  $n > 1$ . Since the drive mixes only adjacent levels, the energy corrections  $\hbar\Delta\omega_{\pm,r}$  arising from second-order perturbation theory to the  $\overline{|+_r\rangle}, \overline{|-_r\rangle}$  energies  $\hbar\omega_{\pm,r}^0$  are

only due to the  $\overline{|2_r\rangle}$  state. These are given by

$$\omega_{\pm,r}^0 = \frac{\delta_{1,r}}{2} \pm \sqrt{\left(\frac{\delta_{1,r}}{2}\right)^2 + \Omega_d^2}, \quad (\text{D7})$$

$$\Delta\omega_{-,r} = 2\Omega_d^2 \frac{\sin^2(\theta_r/2)}{\omega_{-,r}^0 - \delta_{2,r}}, \quad (\text{D8})$$

$$\Delta\omega_{+,r} = 2\Omega_d^2 \frac{\cos^2(\theta_r/2)}{\omega_{+,r}^0 - \delta_{2,r}}. \quad (\text{D9})$$

We can now determine the transition frequencies for the  $|1_p\rangle \rightarrow |3_p\rangle$  ( $\omega_{13,p}$ ) and  $|2_p\rangle \rightarrow |4_p\rangle$  ( $\omega_{24,p}$ ) polariton transitions. In the dispersive regime, the polariton states are given by the mapping  $|1_p\rangle \equiv |-,0\rangle$ ,  $|2_p\rangle \equiv |+,0\rangle$ ,  $|3_p\rangle \equiv |-,1\rangle$ , and  $|4_p\rangle \equiv |+,1\rangle$ . When  $\omega_{\text{coup}} = \omega'_{ge,0}$  (as in Fig. 4), we have  $\delta_{1,0} = 0, \delta_{1,1} = -2\chi$ . Furthermore, we can also approximate  $\delta_{2,0} \approx \delta_{2,1} \approx \alpha \gg \omega_{\pm,r}$ . Then, we obtain

$$\omega_{13,p} = \tilde{\omega}_r - \chi - (\sqrt{\chi^2 + \Omega_d^2} - \Omega_d) + \frac{\Omega_d^2 \cos \theta_1}{\alpha}, \quad (\text{D10})$$

$$\omega_{24,p} = \tilde{\omega}_r - \chi + (\sqrt{\chi^2 + \Omega_d^2} - \Omega_d) - \frac{\Omega_d^2 \cos \theta_1}{\alpha}, \quad (\text{D11})$$

which correspond to Eq. (9) discussed in the paper.

- 
- [1] A. Wallraff, D. I. Schuster, A. Blais, L. Frunzio, R.-S. Huang, J. Majer, S. Kumar, S. M. Girvin, and R. J. Schoelkopf, *Nature* **431**, 162 (2004).
- [2] A. Blais, R.-S. Huang, A. Wallraff, S. M. Girvin, and R. J. Schoelkopf, *Physical Review A* **69**, 062320 (2004).
- [3] J. Q. You and F. Nori, *Nature* **474**, 589 (2011).
- [4] X. Gu, A. F. Kockum, A. Miranowicz, Y. xi Liu, and F. Nori, *Physics Reports* **718–719**, 1 (2017), arXiv:1707.02046.
- [5] R. Schoelkopf and S. Girvin, *Nature* **451**, 664 (2008).
- [6] D. I. Schuster, A. Wallraff, A. Blais, L. Frunzio, R.-S. Huang, J. Majer, S. M. Girvin, and R. J. Schoelkopf, *Physical Review Letters* **94**, 123602 (2005).
- [7] T. Niemczyk, F. Deppe, H. Huebl, E. Menzel, F. Hocke, M. Schwarz, J. Garcia-Ripoll, D. Zueco, T. Hümmer, E. Solano, *et al.*, *Nature Physics* **6**, 772 (2010).
- [8] P. Forn-Díaz, J. J. García-Ripoll, B. Peropadre, J.-L. Orgiazzi, M. A. Yurtalan, R. Belyansky, C. M. Wilson, and A. Lupascu, *Nature Physics* **13**, 39 (2017).
- [9] F. Yoshihara, T. Fuse, S. Ashhab, K. Kakuyanagi, S. Saito, and K. Semba, *Nature Physics* **13**, 44 (2017).
- [10] J. Fink, M. Göppl, M. Baur, R. Bianchetti, P. J. Leek, A. Blais, and A. Wallraff, *Nature* **454**, 315 (2008).
- [11] L. S. Bishop, J. Chow, J. Koch, A. Houck, M. Devoret, E. Thuneberg, S. Girvin, and R. Schoelkopf, *Nature Physics* **5**, 105 (2009).
- [12] B. Suri, Z. Keane, L. S. Bishop, S. Novikov, F. C. Wellstood, and B. S. Palmer, *Physical Review A* **92**, 063801 (2015).
- [13] O. Astafiev, K. Inomata, A. Niskanen, T. Yamamoto, Y. A. Pashkin, Y. Nakamura, and J. Tsai, *Nature* **449**, 588 (2007).
- [14] M. Reed, L. DiCarlo, B. Johnson, L. Sun, D. Schuster, L. Frunzio, and R. Schoelkopf, *Physical review letters* **105**, 173601 (2010).
- [15] L. S. Bishop, E. Ginossar, and S. Girvin, *Physical review letters* **105**, 100505 (2010).
- [16] M. Boissonneault, J. Gambetta, and A. Blais, *Physical review letters* **105**, 100504 (2010).
- [17] M. Baur, S. Filipp, R. Bianchetti, J. M. Fink, M. Göppl, L. Steffen, P. J. Leek, A. Blais, and A. Wallraff, *Physical Review Letters* **102**, 1 (2009), arXiv:0812.4384.
- [18] M. A. Sillanpää, J. Li, K. Cicak, F. Altomare, J. I. Park, R. W. Simmonds, G.-S. Paraoanu, and P. J. Hakonen, *Physical Review Letters* **103**, 193601 (2009).
- [19] Z. H. Peng, J. H. Ding, Y. Zhou, L. L. Ying, Z. Wang, L. Zhou, L. M. Kuang, Y. X. Liu, O. V. Astafiev, and J. S. Tsai, *Physical Review A* **97**, 1 (2018), arXiv:1705.11118.
- [20] H. Ian, Y.-x. Liu, and F. Nori, *Physical Review A* **81**, 063823 (2010).
- [21] K. Murali, Z. Dutton, W. Oliver, D. Crankshaw, and T. Orlando, *Physical review letters* **93**, 087003 (2004).
- [22] H.-C. Sun, Y.-x. Liu, H. Ian, J. You, E. Il'ichev, and F. Nori, *Physical Review A* **89**, 063822 (2014).
- [23] I.-C. Hoi, C. Wilson, G. Johansson, T. Palomaki, B. Peropadre, and P. Delsing, *Physical review letters* **107**, 073601 (2011).
- [24] B. Suri, Z. Keane, R. Ruskov, L. S. Bishop, C. Tahan, S. Novikov, J. Robinson, F. Wellstood, and B. Palmer, *New Journal of Physics* **15**, 125007 (2013).
- [25] S. Novikov, T. Sweeney, J. E. Robinson, S. P. Premaratne, B. Suri, F. C. Wellstood, and B. S. Palmer, *Nature Physics* **12**, 75 (2016).

- [26] B. M. Ann and G. A. Steele, Physical Review A **102**, 1 (2020), arXiv:2005.01975.
- [27] K. Inomata, Z. Lin, K. Koshino, W. D. Oliver, J.-S. Tsai, T. Yamamoto, and Y. Nakamura, Nature communications **7**, 12303 (2016).
- [28] X. Gu, S. N. Huai, F. Nori, and Y. X. Liu, Physical Review A **93**, 1 (2016), arXiv:1601.05148.
- [29] J. Long, H. S. Ku, X. Wu, X. Gu, R. E. Lake, M. Bal, Y. X. Liu, and D. P. Pappas, Physical Review Letters **120**, 1 (2018).
- [30] K. Koshino, K. Inomata, T. Yamamoto, and Y. Nakamura, Physical Review Letters **111**, 1 (2013), arXiv:1306.6695.
- [31] K. Koshino, K. Inomata, T. Yamamoto, and Y. Nakamura, New Journal of Physics **15** (2013), 10.1088/1367-2630/15/11/115010.
- [32] K. Inomata, K. Koshino, Z. R. Lin, W. D. Oliver, J. S. Tsai, Y. Nakamura, and T. Yamamoto, Physical Review Letters **113**, 1 (2014), arXiv:1405.5592.
- [33] K. Koshino, K. Inomata, Z. R. Lin, Y. Tokunaga, T. Yamamoto, and Y. Nakamura, Physical Review Applied **7**, 1 (2017).
- [34] J. Koch, M. Y. Terri, J. Gambetta, A. A. Houck, D. I. Schuster, J. Majer, A. Blais, M. H. Devoret, S. M. Girvin, and R. J. Schoelkopf, Physical Review A **76**, 042319 (2007).
- [35] A. Potts, G. Parker, J. Baumberg, and P. De Groot, IEE Proceedings-Science, Measurement and Technology **148**, 225 (2001).
- [36] H. Risken, *The Fokker-Planck Equation*, edited by H. Haken, Springer Series in Synergetics, Vol. 18 (Springer, Berlin, Heidelberg, 1989).
- [37] S. M. Tan, “A Quantum Optics Toolbox for Matlab 5,” .
- [38] J. R. Johansson, P. D. Nation, and F. Nori, Computer Physics Communications **183**, 1760 (2012).